Advanced Functional Materials

ADVANCED FUNCTIONAL MATERIALS
www.afm-journal.de

RESEARCH ARTICLE OPEN ACCESS

Light-Actuated Fiber-Climbing Inchworm Robot Toward Endoluminal Navigation

Antonio Lobosco[1] | Leilei Song[2] | Fan Liu[2] | Yu-Hsiang Lin[1] | Venkatasubramanian Kalpathy Venkiteswaran[1] | Hao Zeng[2] | Sarthak Misra[1]

[1]Surgical Robotics Laboratory, Department of Biomechanical Engineering, University of Twente, Enschede, The Netherlands | [2]Light Robots, Faculty of Engineering and Natural Sciences, Tampere University, Tampere, Finland

Correspondence: Antonio Lobosco (a.lobosco@utwente.nl) | Sarthak Misra (s.misra@utwente.nl)

Received: 25 February 2026 | **Revised:** 11 April 2026 | **Accepted:** 17 April 2026

Keywords: endoscopic tools | liquid crystal elastomers | photo-actuation | soft robotics | side-emitting optical fibers

ABSTRACT

Light-responsive materials provide unique properties for developing remotely controllable and scalable soft robotic systems. Nevertheless, conventional light-driven systems require a direct line-of-sight and suffer from limited optical field penetration, restricting their use when considering applications in clinically relevant environments. In this work, we address these limitations by integrating wavelength-selective liquid crystalline elastomer (LCE) soft actuators with a tailored side-emitting optical fiber as an endoluminal-compatible platform. The fiber redistributes the input optical energy to the side output, enabling wavelength-selective actuation in individual segments of the soft robot body, and providing physical guidance for controlled locomotion along its surface. Beyond the conventional designs that typically integrate LCEs at the waveguide distal tip only for tip steering or gripping tasks, our system comprises a kirigami-engineered 3D cylindrical architecture fitting around the fiber, and a light-locking mechanism enabled by photothermal deformation of LCEs. This design permits wavelength-selective step motion and amplified out-of-plane deformation for enhanced locomotive efficiency. We show that programmed temporal illumination patterns result in controllable inchworm-like locomotion. This line-of-sight-independent locomotion is suited for future applications in confined endoluminal environments.

1 | Introduction

Photo-responsive smart materials and light-controlled systems have gained significant attention in the field of biomedical engineering, owing to their merits in miniaturization, remote control, capacity of large and reversible deformation, and most importantly, their inherent compatibility with biomedical instrumentation employing high-intensity electromagnetic fields (e.g., magnetic resonance imaging) [1, 2]. These advantages have led to the fast development of miniaturized light-driven soft robots with multiple functions, and intelligent structures capable of navigating and operating in challenging spaces, for example, physiological travel routes (e.g., external auditory canal [3], GI tract [4]) and biologically relevant in vitro environments [5, 6]. Among different light-responsive polymers, liquid crystal elastomers (LCEs) represent a promising class, combining the elasticity inherent in elastomers with the intrinsic anisotropy given by the pre-programmed order in liquid crystalline matters [7–9]. The interplay between this unique molecular architecture, chemical functionalization, and phase transition property gives rise to human-controllable and programmable robotic deformation. By synergizing LCEs with compliant mechanism-based design, such as kirigami or origami, the deformability can be diversified and its amplitude enhanced [10, 11, 12]. Furthermore, it is worth noting that the light-powered strategy can be integrated with intertwined channels of different colors. In other

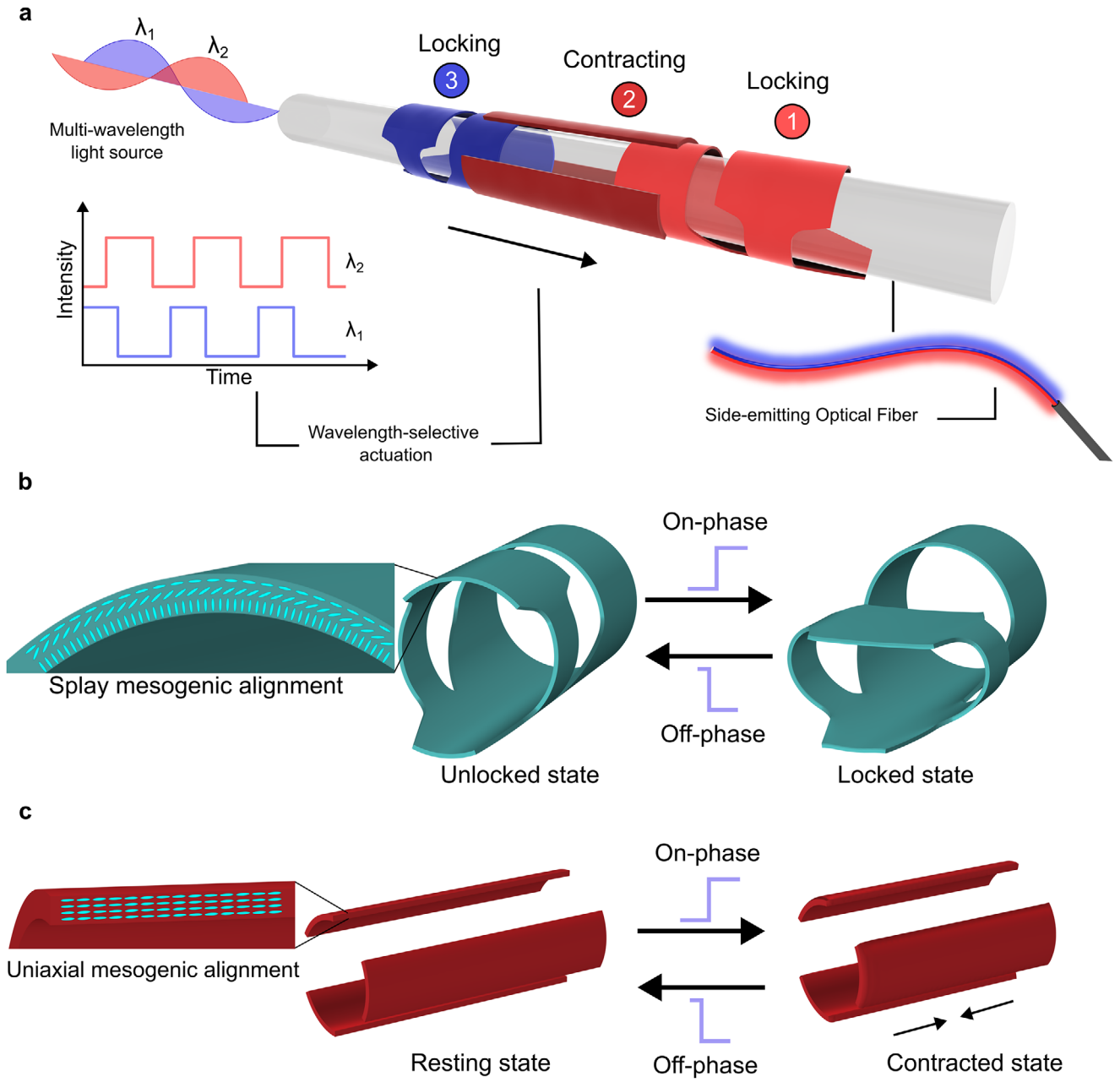

FIGURE 1 | The system design. (a) Schematic of the system components and kirigami-based design. Segments 1 and 2 respond to wavelength 1 (λ_1) = 460 nm (blue), while segment 3 responds to wavelength 2 (λ_2) = 660 nm (red). The numbers correspond to the actuation sequence order, and the arrow indicates the direction of motion. (b) The locking segment transitions from an unlocked to a locked state during the on and off phases of the associated temporal light pattern. The splay-aligned mesogenic configuration of the corresponding liquid crystal elastomer film is illustrated in the inset. (c) The linear actuator transitions from a resting state to a contracted state during on and off phases of the associated temporal light pattern. The uniaxially aligned mesogenic configuration is illustrated in the inset.

words, different wavelengths can be used to deform and actuate distinct LCEs or different segments of a single sample when different light-absorbing dyes are employed [13, 14]. Given the rich chemical diversity of these dyes, light actuation enables multiple degrees of freedom in robotic deformation, which is a key requirement for soft robotics and advanced biomedical engineering [15, 16, 17].

Light-responsive LCEs have been widely used to develop light-driven soft robotic systems in both micro and macroscales. The actuation of such robots conventionally relies on a free-space illumination configuration, where a movable light source and an unobstructed line-of-sight are required. These aspects represent the main challenges when considering future applications in clinically relevant conditions, where the limited penetration of light through biological tissues and the narrow deep-seated working space strongly limit their performance. Nevertheless, existing medical procedures (e.g., endoscopy, fluorescence endomicroscopy, laser ablation, photodynamic therapy) rely on guided light delivered within the human body to face the tortuous anatomical pathways [18–20]. In particular, optical fibers and advanced light delivery systems have shown advantages

in terms of flexibility, dimensions scalability, and versatility in photomedicine and major minimally invasive surgery procedures [21–23]. Conventional clinic-ready optical fibers typically include a light source for illumination and probes for imaging and visualization, or a high-power laser for tumor ablation and vascular surgery [18, 19].

Therefore, harnessing the optical power already present in deep-seated anatomical working spaces by leveraging the synergistic coupling of fiber optics and light-actuated smart materials could extend the functional capabilities of existing light-based medical procedures. This approach may represent a compelling step towards less invasive and more effective treatments, including targeted drug delivery, localized phototherapy, and improved tissue manipulation. Previous works demonstrated the feasibility of coupling light-responsive LCEs with optical fibers or optical waveguides, exploiting the optical power available at their distal end to perform different tasks and therefore developing devices known as waveguide photoactuators [3, 4, 24–27]. Most works focus on steering the orientation of the device tip based on the control of output light intensity from the optical fiber. Nevertheless, no demonstration of robotic movement or locomotion has been reported.

In this work, we present an LCE-based soft kirigami inchworm robot capable of translocation along a 1.5 mm-sized side-emitting optical fiber. The fiber was tailored to provide the optical energy necessary for the robot's propulsion. The robotic system is composed of three soft actuator components functionalized with two different absorbing dyes, which guarantee wavelength-selective actuation and, consequently, sequential control of the individual units. By coupling a multi-wavelength LED light source into the waveguide and applying temporal light patterns, the structure was able to move along the fiber. The results demonstrate how the integration of photonic design, light-responsive smart materials, and compliant mechanisms could lead to deployable light-driven soft robotic systems for future endoluminal applications.

2 | Results and Discussion

2.1 | System Concept

The soft inchworm robot features a three-segment structure, two locking components, and a contracting linear actuator, able to harness the optical energy delivered by the light refracted from a customized side-emitting plastic optical fiber (i.e., SEOF) (Figure 1a). The SEOF fabrication process details are reported in the Experimental Section. A multi-wavelength LED light source was coupled to the SEOF, guiding a temporal light pattern for two specific wavelengths corresponding to the related absorption peaks of the dye-functionalized robot components. The first locking component and the linear actuator were dyed with Disperse Red 1 (DR1) and can be selectively actuated by blue light at 460 nm, while the second locking component, dyed with Disperse Blue 14 (DB14), selectively responds to red light (660 nm). The wavelength-selective actuation allows for the sequential movement necessary for inchworm-like locomotion. When the blue light is in its on phase, the first locking component (1, Figure 1a) locks around the fiber, and the linear actuator (2, Figure 1a) contracts simultaneously, pulling the robot toward the locking point. Then, the red light is turned on, actuating the second locking component (3, Figure 1a), which anchors the rear part of the robot. The first locking component then unlocks as the blue light turns off, allowing the robot's body to extend through the relaxation of the linear actuator. After turning off the red illumination, the robot unlocks and completes one inching cycle. This entire sequence is achieved using LCE film-based components, where the locking segments transition from an unlocked state to a locked state by bending upon illumination (Figure 1b), and the linear actuator transitions from a resting state to a contracted state (Figure 1c). To achieve the above-mentioned transitions, films with two different mesogenic alignments were used. The locking mechanism relies on the splay-aligned films where the orientation of mesogens varies across the film thickness (50 μm), ranging from planar (mesogens parallel to the film surface) to homeotropic (mesogens perpendicular to the film surface) configurations. The locking segments were developed keeping the homeotropic and planar regions at the inner and outer sides of the structure, respectively. Upon illumination, the planar region contracts while the homeotropically aligned region expands, resulting in the squeezing of the ring-shaped structure around the SEOF (Figure 1b, locked state). The bending of the LCE actuator is caused by a reduction in the order parameter within the liquid crystalline network, without the need to overcome the nematic-to-isotropic phase transition, which occurs at a relatively high temperature in this type of chemical [28]. The linear actuator is composed of three equal uniaxially-aligned LCE segments (100 μm in thickness), each exhibiting unidirectional contraction along the SEOF axis upon illumination (Figure 1c). The contraction is driven by a nematic-to-isotropic phase transition, and additional details regarding the characterization of the heat-induced phase transition for the uniaxially aligned LCE films are reported in Figure S1.

2.2 | Simulation-Driven Design and Fabrication Process

The Kirigami-based fabrication process of the soft robotic system is illustrated in Figure 2a. It involves laser cutting of the dyed LCE films, followed by the assembly of the obtained segments and then by rolling them into a cylindrical structure. Finite element method (FEM) simulations were conducted to qualitatively assess the influence of geometrical parameters on the actuation performance of the single components. The fabrication process and FEM simulations details are reported in the related Experimental Section. The locking segment design with the related geometrical parameters and the FEM-predicted deformed configuration are reported in Figure 2b. The design includes two soft flexure hinges, with length and width defined by L_H and W_H parameters, which enable the central actuation segment, characterized by L_B and W_B, to bend inwards. It is worth noting that L_H and L_B are interdependent due to constraints imposed by the fixed fiber circumference and the extent of the overlapping regions necessary for the fabrication.

The ratios L_H/L_B and W_H/W_B were employed as design parameters to evaluate the maximum inward displacement achieved across different design configurations. This approach enabled the identification of the most efficient geometry for inducing squeezing around the fiber under the same actuation conditions. The

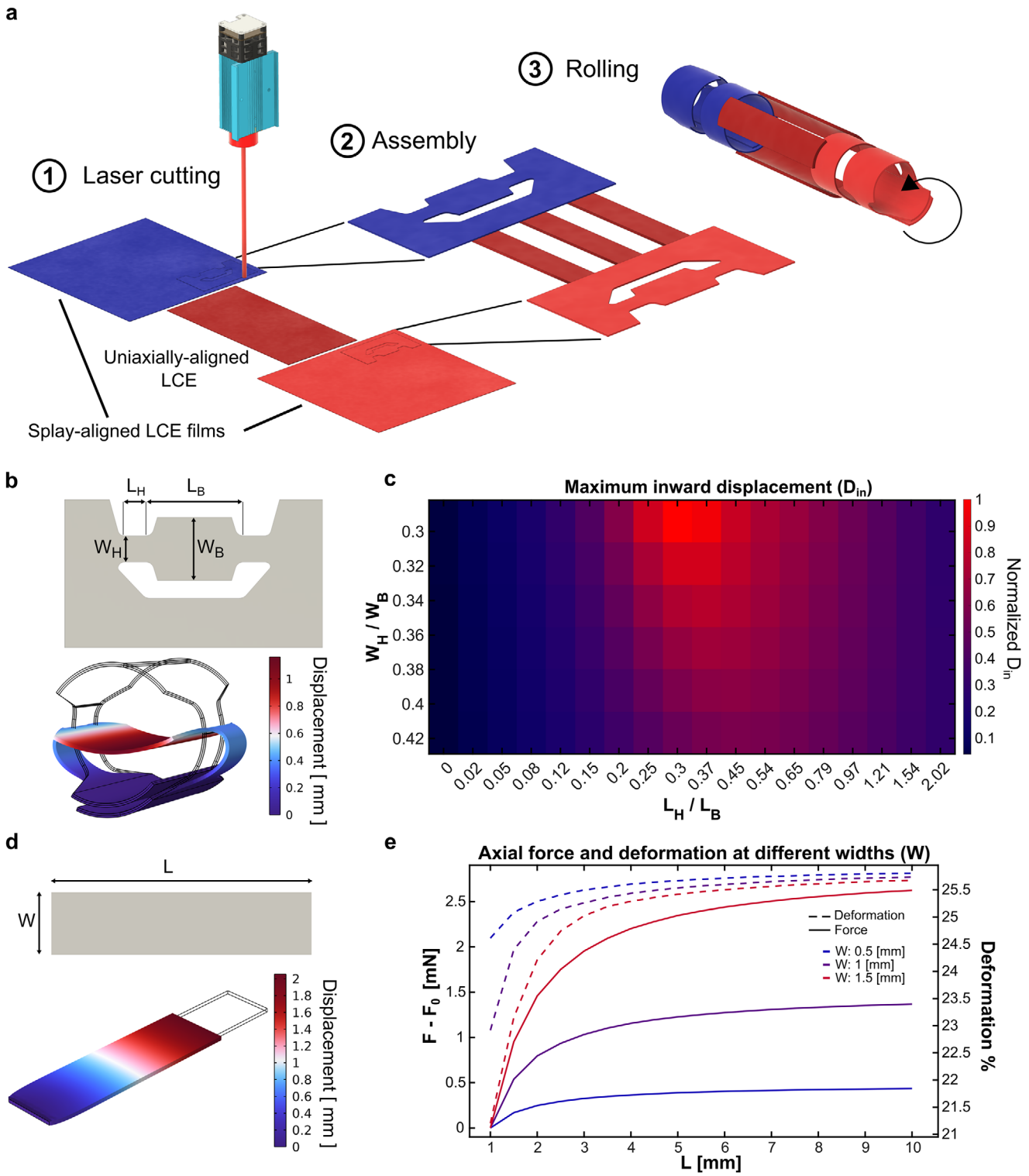

FIGURE 2 | Fabrication process and Kirigami design parameters. (a) Fabrication process involving three main steps: 1-Laser cutting of dye-functionalized liquid crystal elastomers (LCE) films; 2-Assembly of the planar structures obtained from the laser cutting process; 3-Rolling of the 2D assembly, resulting in a 3D cylindrical soft robotic system. (b) 2D geometry of the locking segments with the main design parameters. L_H, W_H: flexure hinge length and width, respectively. L_B, W_B: central actuation segment length and width, respectively. Finite element method (FEM) simulation results, showing the displacement magnitude field in the deformed configuration. (c) Parametric heatmap indicating the L_H/L_B and W_H/W_B values to achieve maximum inward displacement (D_{in}). The heatmap shows the value of (D_{in}) normalized by its maximum value. (d) 2D geometry of one segment of the linear actuator with the related design parameters. L, W: length and width of the segment, respectively. FEM simulation results show the displacement magnitude field in the deformed configuration. (e) FEM simulation results for axial forces (solid lines) and deformation (dashed lines) for different geometrical parameters values.

parametric heatmap in Figure 2c shows the normalized inward displacement (D_{in}) dependency over L_H/L_B and W_H/W_B ratios. The maximum D_{in} occurs for intermediate values of L_H/L_B ($\approx$ 0.3 – 0.45) at fixed W_H/W_B values, suggesting that excessively long flexure hinges reduce the effective length of the central actuation segment, therefore limiting its bending capability. Conversely, the short flexure hinge imposes strong constraints at both ends of the segment, limiting its inward displacement. The parametric heatmap indicates that the inward displacement strongly depends also on W_H/W_B ratio, with peak values occurring at relatively low ratios (≈0.3–0.32). This suggests that configurations with narrower hinge-to-central segment width proportions lead to higher inward displacements, highlighting the need for tailored geometry to achieve optimal actuation.

Figure 2d reports the design with the related geometrical parameters and FEM simulations predictions of one segment of the linear actuator. Configurations with different width (W) and length (L) values were simulated (Figure 2e), comparing the resulting percentage deformation (dashed lines) and the axial forces (solid lines) exerted by the contracting segment. Narrower segments exhibit higher deformation at low L values, but the dependency over widths becomes smaller as L increases. This is not the case for the axial forces, which strongly depend on the segment width. This means that it is possible to prioritize width for force efficiency without sacrificing significant displacement. Therefore, finding a trade-off between force and deformation is essential for tailoring the soft linear actuator to specific applications requiring either high displacement or high load-bearing capability.

2.3 | Characterization of Soft Robotic Individual Components

The actuation of the individual soft robotic components was characterized under external illumination to determine their wavelength selectivity and to validate the deformation patterns predicted by the FEM simulations. The actuation sequence for a single DR1-functionalized segment of the linear actuator and the related actuation performance are reported in Figure 3a-i–vi,b,c, respectively. Figure 3b shows the time-dependent deformation measured during one light on/off cycle upon illumination at two different wavelengths, 460 and 660 nm. The sample exhibited significantly higher deformation upon illumination at 460 nm than at 660 nm, demonstrating strong wavelength selectivity. This is extensively supported by the measurements reported in Figure 3c, where the maximum deformation was recorded at different irradiance levels for both wavelengths. The maximum deformation achieved with 460 nm illumination is ∼5 times higher than the case of 660 nm, considering the same irradiance values. Figure 3d reports the actuation sequence for the locking segment upon external illumination. In particular, Figure 3d-ii shows the inward displacement resulting from the bending of the central actuation segment as predicted from the qualitative simulations (Figure 2b). The displacement dynamics are reported in Figure 3e, including both DR1- and DB14-functionalized locking segments, under illumination at both wavelengths (460 and 660 nm). Each locking segment exhibits higher displacement values and faster response when illuminated at its corresponding absorbing wavelength. The maximum inward displacement was then measured at the two actuation wavelengths and for different irradiance values, as reported in Figure 3f. The two locking segments achieve higher displacement values for increasing irradiance values. The top plot (Figure 3f) reports their response under illumination at 460 nm, showing higher displacement values for the DR1-functionalized segment than the DB14-functionalized segment at equal irradiance values, demonstrating wavelength selectivity. The bottom plot (Figure 3f) shows their response under illumination at 660 nm. As in the previous case, the displacement values increase by increasing the irradiance. Additionally, an increase in wavelength selectivity (in terms of displacement difference between the two curves evaluated at the same irradiance) for increasing irradiance values can be noticed. Considering both, the DB14-functionalized segment exhibits an increased response at its non-corresponding wavelength compared to that of the DR1-functionalized segment, indicating lower wavelength selectivity.

Nevertheless, these results strongly support the wavelength-selective response of the individual soft robotic components and confirm the deformation pattern predicted by the FEM simulations.

2.4 | Actuation Enabled by Side-Emitting Optical Fiber

After assessing the actuation performance of the individual robot segments, the inchworm motion of the soft robot was investigated using a SEOF as the light source. The SEOF was obtained by laser processing a 1,5 mm sized plastic optical fiber (Figure S2a, Experimental section) to perform V-shaped notches that allow for lateral light refraction (Figure 4a). The notch parameters (Figure 4a-i) were optimized to control lateral light refraction and to obtain an equalized intensity profile along the fiber. Figure 4b reports the axial intensity profiles of the SEOF before and after design optimization. The non-optimized SEOF features notches with constant width and depth dimensions along the fiber segment, while the optimized configuration included a gradient both in width and depth dimensions. They were designed to ensure that the average irradiance of the laterally refracted light over the fiber surface was comparable to that obtained with external illumination (Figure S2b, Experimental Section). The uniform light intensity profile along the SEOF segment guarantees that enough optical energy is available for the actuation of each robot component along the fiber.

The actuation sequence of the inchworm robot along the SEOF is reported in Figure 4c-i–vi. The driving signal consists of two square wave temporal light patterns, each of which related to a specific wavelength. The parameters of the temporal light patterns (e.g., period, delay, and duty cycle), reported in the Experimental section, were selected based on the deformation and displacement dynamics of the contracting and locking segments shown in Figure 3b,e, respectively. Additional details on the photothermal actuation and on how the temporal light patterns relate to the temperature distribution of each segment during SEOF-driven actuation are reported in Figure S2 and Video S3. The sequence reported in Figure 4c refers to one inching cycle, and each frame corresponds to a specific cycle phase. Figure 4d reports the displacement of the individual locking segments and the contraction of the linear actuator

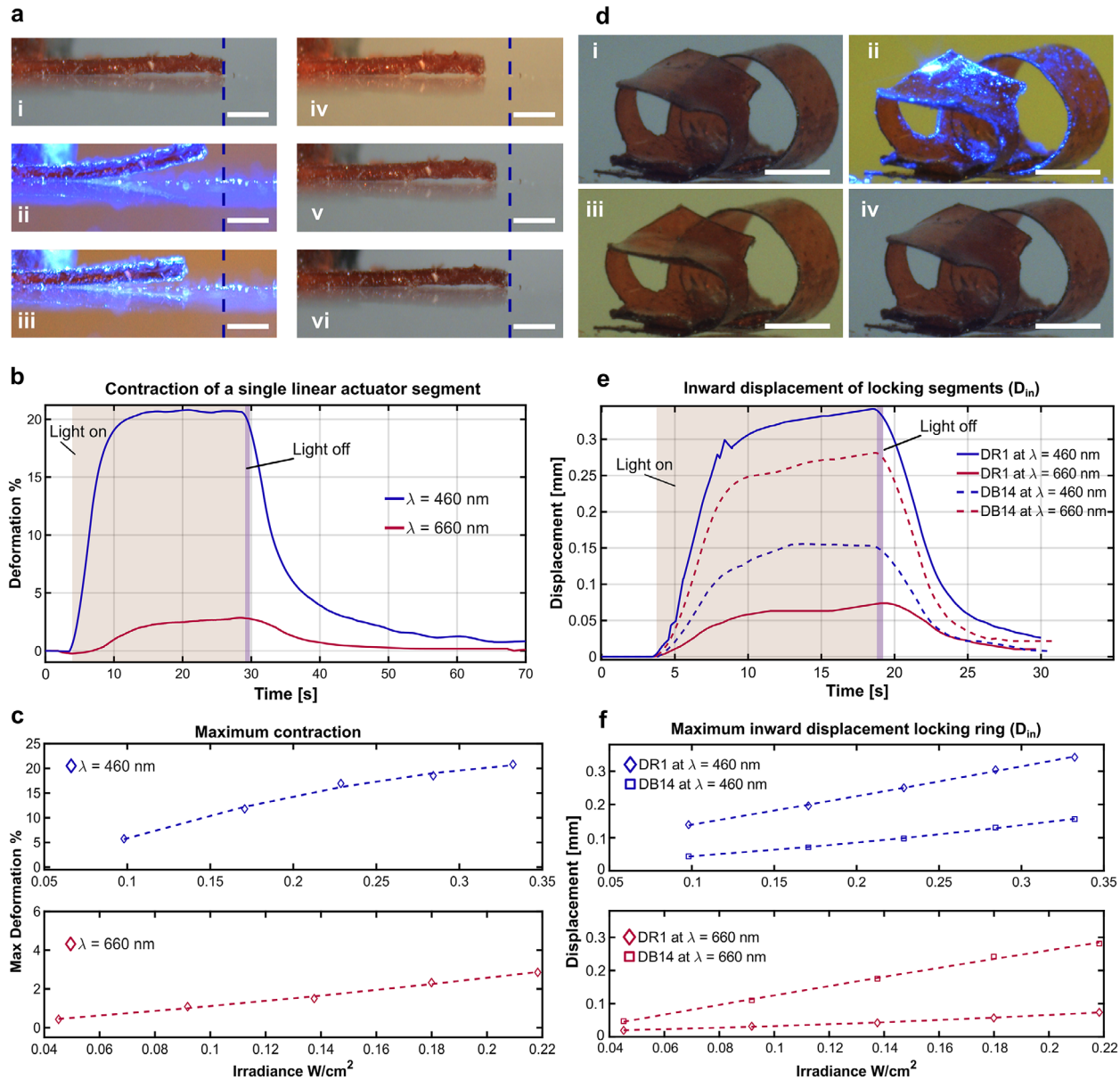

FIGURE 3 | Wavelength-selective actuation of single components through external illumination. (a) Actuation sequence (i–vi) for one segment of the linear actuator. The dashed line indicates the starting position of the free distal end (scale bar: 0.5 mm). (b) Contraction dynamics for a single segment of the linear actuator at the maximum illumination power. (c) Maximum contraction at different irradiance levels. (d) Exemplary actuation sequence (vii–x) for one locking segment (scale bar: 1 mm). (e) Inward displacement dynamics during light on/off cycles for disperse red 1 (DR1) and disperse blue 14 (DB14)-functionalized locking segments (continuous and dashed curves, respectively) at wavelengths of 460 and 660 nm. The inward displacement was evaluated by tracking the middle point of the central actuation segment over time during on/off illumination cycles. (f) Maximum inward displacement for DR1 and DB14-functionalized locking segments as a function of the irradiance and wavelength (460 and 660 nm).

during the actuation through multiple driving cycles. Figure 4e shows a zoom-in view of the highlighted sample cycle. Each phase is distinguished by a different color and is labelled with the corresponding frame shown in Figure 4c. When blue light (λ_1) is on, the front locking segment (DR1, red) anchors at the fiber surface. The rear locking segment (DB14, blue) is unlocked and is pulled forward (~0.6 mm displacement) by the contraction of the linear actuator (dashed lines). Then the red light (λ_2) is turned on to actuate the rear locking segment while the blue light is still on. This helps to prevent slippage of the front locking segment and keeps the linear actuator contracted until the rear locking segment gets fully anchored. At this point, the blue light is turned off, allowing the front locking segment to unlock and the linear actuator to elongate until the next cycle starts (Video S1).

The motion resulting from successive driving cycles leads to a stepwise displacement of the locking segments and the alternating contraction/elongation of the linear actuator (Figure 4d). This reflects the inchworm-like locomotion of the soft robot (Video S2). This behavior resembles previously reported systems that feature different actuation principles (e.g., pneumatic, electric, magnetic) and materials [29, 30]. Figure 4d and Video S2 reveal that, after the first two cycles, slight slippage of the locking segments occurs, particularly in the DB14-functionalized segment. In addition, the

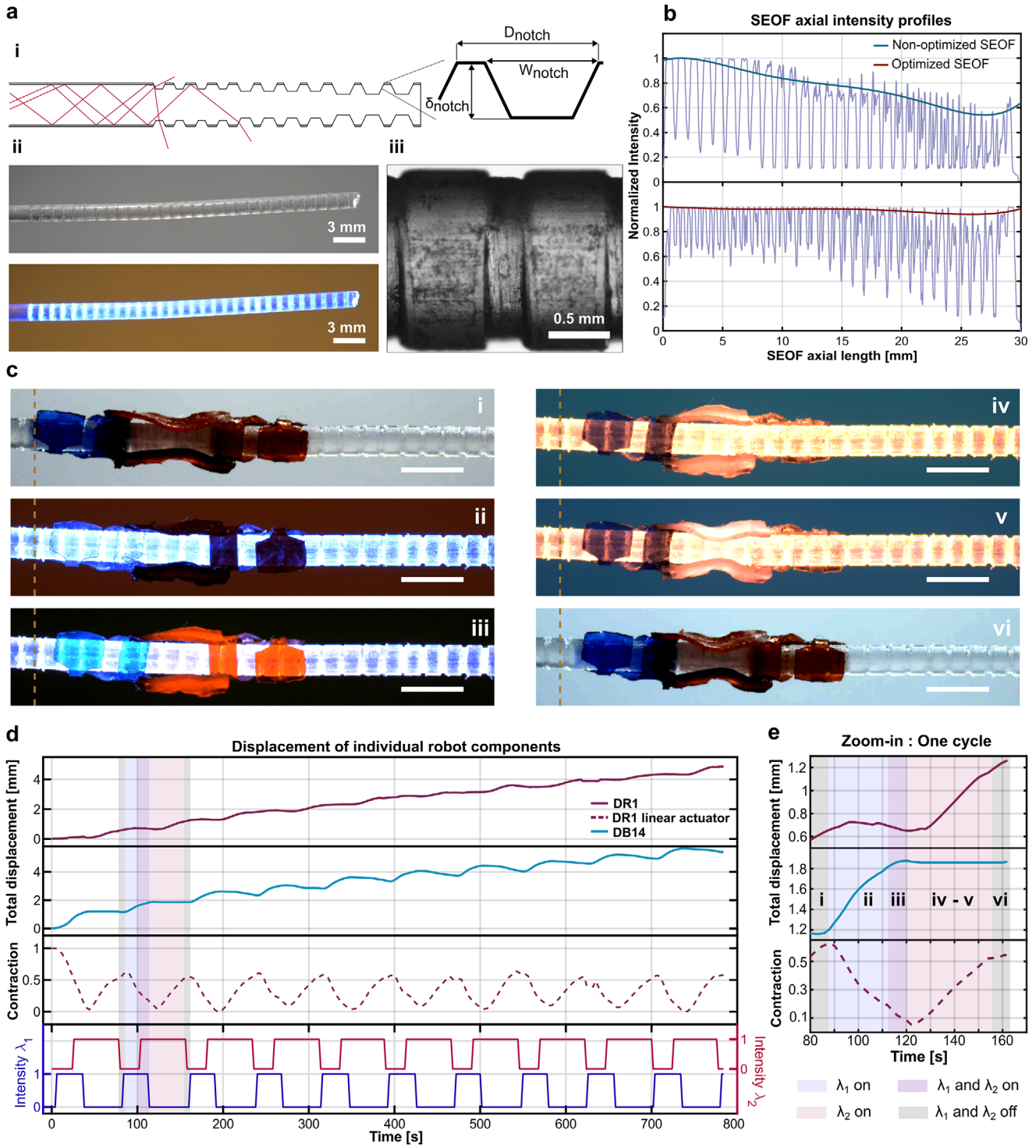

FIGURE 4 | Soft Robotic Inchworm Actuation Enabled by Side-Emitting Optical Fiber (a) Schematic of a notched side-emitting optical fiber (SEOF) and the related key design parameters (i). Images of the fabricated SEOF, light off (ii, top) and light on (ii, bottom), showing light being refracted outside the optical fiber core. Exemplary microscopy image of the notches obtained by laser engraving procedures (iii). (b) Normalized axial intensity profiles of SEOFs with non-optimized (top) and optimized (bottom) notch parameters. Continuous lines represent the fitted envelopes of the measured profiles, illustrating the intensity profile of side-emitted light along the fiber length. (c) Frame-by-frame sequence of the inchworm robot for one actuation cycle (i–vi, scale bar: 3 mm). The dashed line indicates the original position of the robot. Frames are extracted from Video S2. (d) Displacement of individual robot components along the fiber during actuation under a pulsed temporal light pattern transmitted through SEOF (scale bar: 3 mm). The contraction values are reported after baseline removal and normalization, where 1 corresponds to the full original length and 0 to the fully contracted state. (e) Enlarged view of a single actuation cycle, with each color representing a distinct actuation phase. For each phase, the corresponding frames are labeled (i–vi).

current system is limited by the unidirectionality of the robot translocation. This constraint arises primarily from the limited wavelength-selective responsiveness of the dyes used for LCE film functionalization, which reduced the available options for a suitable third dye that could have been used to functionalize one of the robot segments, enabling individual control of each segment and, consequently, bidirectional translocation.

3 | Conclusion

This work presents a light-actuated soft inchworm robot capable of harnessing optical energy from a customized SEOF to sustain its locomotion. By integrating wavelength-selective LCE-based kirigami components and combining different mesogenic alignments with geometry-optimized locking and actuation segments, the robot achieves controlled, sequential fiber-climbing locomotion. FEM analysis guided the selection of geometrical parameters to maximize actuation performance. Leveraging kirigami techniques and the inherent flexibility of these materials, we developed a soft cylindrical robotic structure tailored to a specific optical-fiber dimension, demonstrating the feasibility of creating fully customized systems that can be adapted to different sizes. Such a design is particularly relevant for applications in confined or tubular environments where current light-driven soft robots struggle to operate. However, important limitations in terms of actuation effectiveness, speed, and the unidirectionality of robot's translocation are noticed. Furthermore, this study focuses exclusively on actuation in air, without addressing performance in liquid environments where optical energy absorption efficiency and locomotion capabilities might be significantly altered. Future development of improved LCE formulations with higher photothermal or photomechanical conversion efficiency, suitable dyes with sharp and distinct absorption spectra, and mechanical design could lead to enhanced performance and improved functionalities, overcoming current challenges. Despite these limitations, the proposed approach highlights the potential of LCE-based soft robots to be integrated with fiber-based endoluminal illumination systems. The ability to convert guided light into controlled motion of a soft robotic system directly at the distal end of a side-emitting optical fiber opens potential pathways for the development of future multifunctional optical-fiber-integrated robotic systems for biomedical applications, including targeted tissue manipulation, localized drug delivery, and endoluminal navigation.

4 | Experimental Section

4.1 | Materials

A plastic optical fiber was purchased from Edmund Optics (02-535 1500 µm, Optical Grade Plastic Optical Fiber Unjacketed). 1,4-Bis-[4-(6-acryloyloxyhexyloxy)benzoyloxy]-2-methylbenzene (99%, RM82) and 1,4-Bis-[4-(3-acryloyloxypropyloxy)benzoyloxy]-2-methylbenzene (97%, RM257) were purchased from SYNTHON Chemicals. 6-amino-1-hexanol (97%), dodecylamine (97%), and DPA (dipropylamine) were purchased from TCI. Disperse Red 1 (95%), Disperse Blue 14 (97%), EDDT (2,2′-(ethylenedioxy)diethanethiol), PETMP (pentaerythritol tetrakis(3-mercaptopropionate)), BHT (2,6-di-tert-butyl-4-methylphenol), and Irgacure 651 (2,2-dimethoxy-2-phenylacetophenone) were purchased from Sigma-Aldrich. UV-curable adhesive was purchased from Norland (UVS 91).

4.1.1 | The LCE for the Locking Segments

To prepare liquid crystal cells, two glass substrates were bonded together using spacers to determine the gap. One substrate was coated with polyvinyl alcohol (PVA, 5 wt% in water, 3000 RPM, 1 min) and baked at 90°C for 10 min, and then unidirectionally rubbed to attain uniaxial alignment in LC. The other substrate was coated with polyimide (PI, 3000 RPM, 1 min), followed by baking at 180°C for 20 min to attain homeotropic alignment. For spacers 50 µm microspheres (Thermo Scientific) were used. The liquid crystal mixture contains 0.72 mmol RM 82, 0.20 mmol 6-amino-1-hexanol, 0.20 mmol dodecylamine, and 2.0 wt.% 2,2-dimethoxy-2-phenylacetophenone (Irgacure 651). The mixture was melted (100°C) and infiltrated into the cell at 100°C. After cooling to 65°C (1°C min^{-1}), the cells were stored in an oven at 63°C for 24 h to conduct the aza-Michael addition reaction for generating oligomers. Then, the samples were irradiated with UV light (365 nm, 180 mW cm^{-2}, 10 min) for polymerization. Finally, the cells were opened with a razor blade. 1 mg of Disperse Red 1 (DR1) dye powder or Disperse Blue 14 dye (DR14) powder was spread onto the surface of the samples and thermally diffused into the material on a hot plate at 100°C for 10 min.

4.1.2 | The LCE for the Contracting Segment

To prepare the liquid crystal cells, glass slides were first spin-coated with a 5 wt.% aqueous solution of polyvinyl alcohol (PVA) and subsequently dried at 90°C. Two coated glass slides were then assembled into a cell using 250 µm spacers. In the first step, 0.55 mmol RM257, 0.30 mmol EDDT, and 0.10 mmol PETMP were mixed uniformly at 80°C together with 0.5 wt.% DPA, 1 wt.% BHT, and 1.5 wt.% Irgacure 651 (I651). The LC mixture was filled into the cells, which were then transferred to an oven at 60°C for 24 h to form an LCE prepolymer. In the second step, the cells were immersed in water for 12 h to remove the surface PVA layer. The LCE prepolymer samples were then carefully removed and uniaxially stretched to induce a monodomain alignment, followed by UV polymerization (365 nm, 180 mW cm^{-2}, 15 min) to form LCE films. Finally, the films were immersed in a DR1/isopropanol solution for dyeing.

4.2 | Kirigami-Based Robot Fabrication and Assembly

The robot components were designed in Autodesk Fusion 360 using the sheet metal module by defining custom sheet metal rules to simulate the folding of the 2D-designed structure. The obtained design was imported in Inkscape and then sent to the laser cutter (Speedy 300, Trotec Laser, Marchtrenk, Austria). The laser power was set to 6% of the maximum ($P_{MAX} = 30\ W$). The cutting speed was set to 0.5% of the maximum ($V_{MAX} = 3.55\ m/s$). Other parameters were set as default. After the laser cutting process, the components were detached from the substrate by means of a blade and tweezers and then folded into a cylindrical

shape using a multi-material 3D-printed rod with a rubber-like surface on one side to facilitate film adhesion during the rolling procedure. After the folding, the structures' free extremities were glued using an UV-curable glue (NOA 63).

4.3 | Characterization of the Actuation Performance

Videos and images were acquired by an industrial camera (Ximea GmbH, MC031CG-SY) to characterize kirigami-structures' actuation performances and the inchworm motion of the robot when actuated by the side-emitting optical fiber. A multi-wavelength LED light source (pE-4000, CoolLED Ltd.) coupled to a collimator through a liquid light-guide was used to actuate the photo-responsive LCE kirigami structures for the characterization under external illumination conditions. The recorded videos were then further analyzed with custom MATLAB (R2025a) scripts to track structure displacement upon light excitation. The linear actuator displacement was evaluated by means of a custom algorithm based on adaptive thresholding and a bounding box approach. The actuation performance of the locking component was evaluated by tracking the inward displacement of the central actuation segment using a gradient thresholding algorithm. A Kernelized Correlation Filter (KCF) tracking algorithm was used to track the displacement of the individual robot components during motion along the side-emitting optical fiber.

4.4 | Thermographic Analysis of the Actuation Performance

The side-emitting optical fiber (SEOF) was coupled to a multi-wavelength LED light source (pE-4000, CoolLED Ltd.). Thermographic images were recorded by means of a thermographic camera (Fluke Ti 400, Fluke Corporation) while a temporal light pattern was shone through the SEOF. The waveform parameters of the temporal light pattern were the same used for the inchworm actuation demonstration reported in Figure 4d. Waveform parameters:

- Period: 85 seconds (for both wavelengths, λ_1 and λ_2)
- Delay: 5 seconds for λ_1, 25 seconds for λ_2
- Duty cycle: 35% for λ_1, 62% for λ_2
- Peak Intensity: 100% of the maximum intensity value for both wavelengths
- Low Intensity: 0% of the maximum intensity value for both wavelengths

4.5 | LCE Kirigami Structures Simulation

Simulations were performed using the Structural Mechanics Module of COMSOL Multiphysics. The LCE was modeled using a Gent model, and the material parameters were obtained from Chehade et al. [31]. The thermal response of the LCE films was simulated as previously reported [32]. Bending films were modeled as bimorph structures. Temperature-dependent external stretches were imposed within each layer according to predefined reference frames and considering the axis related to the nematic director's direction.

4.6 | Optical Fiber Functionalization and Characterization

The optical fiber was functionalized by introducing small v-notch cuts through the cladding layer and cladding/core interface using a laser cutter. The fiber was placed in a slit obtained within a PMMA support to prevent movement and keep it in a planar position during laser cutting. The laser cutter was the same used for the fabrication of robot components. The fiber was functionalized over a segment of 3 cm in length. Notch spacing and geometrical parameters (i.e., width and depth) were optimized to achieve a uniform irradiance along the fiber length. The final configuration included a gradient both in width and depth dimensions of the notches over the functionalized segment: The width ranged from 150 to 350 μm with an increase of 50 μm each 6 notches, while the depth was controlled by varying the laser energy deposited, that is, decreasing of 0.05% the laser scanning velocity from 0.5% to 0.4% each 10 notches and maintaining a constant laser power of 1% of the maximum available power.

The optical fiber characterization was performed by acquiring images of the functionalized segment through Ximea digital camera. The intensity profiles over the fiber's segment were estimated and evaluated from these images using a custom MATLAB (R2025a) script.

To estimate the total side-emitted optical power (P_{SE}), a thermal power sensor (S175C, Thorlabs, Inc.) connected to an optical power meter (PM400, Thorlabs, Inc.) was used. The estimation was done according to the following procedure:

1. The optical power input (P_{IN}) was estimated by measuring the power output of a short pristine optical fiber segment. In this way, inherent losses could be neglected, and other losses due to reflections, optical fiber numerical aperture could be included in the measurement.
2. The inherent power loss of the non-functionalized fiber segment (P_{LOSS}) was evaluated considering the attenuation graphs reported in the optical fiber datasheet.
3. The optical power output at the distal end of the side-emitting segment (P_{OUT}) was measured by placing a circular diaphragm between the sensor and fiber output. In this way, only the end-emitted light contributed to the measurement.
4. Then, the following formula was used: $P_{SE} = P_{IN} - P_{LOSS} - P_{OUT}$

The estimated irradiance values are reported in Figure S1c.

Acknowledgements

S.M. and A.L. acknowledge funding from European Research Council (ERC) under the European Union's Horizon 2020 Research and Innovation Program (Grant No. 866494, project-MAESTRO). H.Z. thanks the

ECIU research mobility fund. The authors thank Jianfeng Yang from Tampere University for his support in experiments and LCE knowledge.

Funding

S.M. and A.L. acknowledge funding from European Research Council (ERC) under the European Union's Horizon 2020 Research and Innovation Program (Grant Nr. 866494, project-MAESTRO). H.Z. thanks the ECIU research mobility fund.

Conflicts of Interest

The authors declare no conflicts of interest.

Data Availability Statement

The data that support the findings of this study are available from the corresponding authors upon reasonable request.

References

1. C. Lin, M. Yang, F. Zhang, Y. Liu, and J. Leng, "Stimuli-Responsive Smart Materials for Biomedical Applications," *Materials Science and Engineering: R: Reports* 167 (2026): 101126.

2. Y. Huang, Q. Yu, C. Su, J. Jiang, N. Chen, and H. Shao, "Light-Responsive Soft Actuators: Mechanism, Materials, Fabrication, and Applications," *Actuators* 10 (2021): 298.

3. C. Zhou, Z. Xu, Z. Lin, et al., "Submillimeter Fiber Robots Capable of Decoupled Macro-Micro Motion for Endoluminal Manipulation," *Science Advances* 10 (2024): adr6428.

4. J. Luo, H. Liu, Y. He, et al., "Biocompatible Liquid Crystal Elastomer Optical Fiber Actuator for In Vivo Endoscopic Navigation and Laser Ablation Therapy," *Advanced Materials* 38 (2026): 16047.

5. M. F. Jamil, M. Pokharel, and K. Park, "Light-Controlled Microbots in Biomedical Application: A Review," *Applied Sciences* 12 (2022): 11013.

6. M. Hussain, E. I. L. Jull, R. J. Mandle, T. Raistrick, P. J. Hine, and H. F. Gleeson, "Liquid Crystal Elastomers for Biological Applications," *Nanomaterials* 11 (2021): 813.

7. J. M. Speregen and T. J. White, "Liquid Crystalline Elastomers in Soft Robotics: Assessing Promise and Limitations," *Advanced Robotics Research* (2025): 202500150.

8. T. J. White and D. J. Broer, "Programmable and Adaptive Mechanics With Liquid Crystal Polymer Networks and Elastomers," *Nature Materials* 14 (2015): 1087–1098.

9. E. R. Blackert, P. Scaccia, M. Barnes, et al., "Spatiotemporally Controlled Soft Robotics With Optically Responsive Liquid Crystal Elastomers," *Advanced Intelligent Systems* 7 (2025): 2500045.

10. J. Chen, A. S. Johnson, J. Weber, O. I. Akomolafe, J. Jiang, and C. Peng, "Programmable Light-Driven Liquid Crystal Elastomer Kirigami With Controlled Molecular Orientations," *Advanced Intelligent Systems* 4 (2022): 2100233.

11. Y. Cheng, H. Lu, X. Lee, H. Zeng, and A. Priimagi, "Kirigami-Based Light-Induced Shape-Morphing and Locomotion," *Advanced Materials* 32 (2020): 1906233.

12. S. Liu, Q. Yang, X. Wang, et al., "Untethered Cylindrical Liquid Crystal Elastomer Actuators Based on Centrifugal Fabrication Process," *Chemical Engineering Journal* 512 (2025): 162406.

13. X. Zhang, L. Yao, H. Yan, et al., "Optical Wavelength Selective Actuation of Dye Doped Liquid Crystalline Elastomers by Quasi-daylight," *Soft Matter* 18 (2022): 9181–9196.

14. J. E. Marshall and E. M. Terentjev, "Photo-Sensitivity of Dye-Doped Liquid Crystal Elastomers," *Soft Matter* 9 (2013): 8547.

15. F. Shiralipour, Y. Nik Akhtar, A. Gilmor, G. Pegorin, A. Valerio-Aguilar, and E. Hegmann, "The Role of Liquid Crystal Elastomers in Pioneering Biological Applications," *Crystals* 14 (2024): 859.

16. W. Zhang, Y. Nan, Z. Wu, Y. Shen, and D. Luo, "Photothermal-Driven Liquid Crystal Elastomers: Materials, Alignment and Applications," *Molecules* 27 (2022): 4330.

17. Q. Yang, X. Wang, Y. Tang, et al., "Four-Waveband-Modulated Liquid Crystal Elastomer (LCE) Actuators for Soft Robotics Based on Optical Wavelength Selective Actuation of Dye-Doped LCE Materials," *Chemical Engineering Journal* 529 (2026): 172892.

18. T. Tsukamoto, Y. Fujita, M. Shimogami, et al., "Inside-the-Body Light Delivery System Using Endovascular Therapy-based Light Illumination Technology," *eBioMedicine* 85 (2022): 104289.

19. G. Keiser, *Biophotonics: Concepts to Applications* (Springer Singapore, 2016).

20. S. Pearson, J. Feng, and A. Del Campo, "Lighting the Path: Light Delivery Strategies to Activate Photoresponsive Biomaterials In Vivo," *Advanced Functional Materials* 31 (2021): 2105989.

21. Y. Hu, P. Minzioni, J. Hui, S. Yun, and A. K. Yetisen, "Fiber Optic Devices for Diagnostics and Therapy in Photomedicine," *Advanced Optical Materials* 12 (2024): 2400478.

22. Y. Guo, J. Zheng, Z. Wang, G. Chen, K. Hou, and M. Zhu, "Biocompatible Optical Fiber for Photomedical Application," *Giant* 16 (2023): 100195.

23. Z. Guang, C. He, V. Bry, A. Le, J. DeMarco, and I. J. Chetty, "Optical Fiber Sensing Technologies in Radiation Therapy," *Photonics* 12 (2025): 1058.

24. O. M. Wani, H. Zeng, and A. Priimagi, "A Light-Driven Artificial Flytrap," *Nature Communications* 8 (2017): 15546.

25. C. Cheng, C. Chen, C. Li, et al., "Fiber-Tip Microgripper With Sub-Milliwatt Photoactuation," *Advanced Optical Materials* 13 (2025): 2402565.

26. M. Xi, H. Pan, Y. Zong, Y. Mei, and J. Cui, "Waveguide Photoactuators: Materials, Fabrication, and Applications," *Advanced Robotics Research* (2025): 202500148.

27. H. Liu, Y. He, J. Luo, et al., "Multimodal Actuation and Precise Control in Liquid Crystal Elastomer Optical Fiber Artificial Muscles," *Advanced Materials* 37 (2025): 05776.

28. R. S. Kularatne, H. Kim, J. M. Boothby, and T. H. Ware, "Liquid Crystal Elastomer Actuators: Synthesis, Alignment, and Applications," *Journal of Polymer Science Part B: Polymer Physics* 55 (2017): 395–411.

29. C. Tang, B. Du, S. Jiang, et al., "A Pipeline Inspection Robot for Navigating Tubular Environments in the Sub-Centimeter Scale," *Science Robotics* 7 (2022): abm8597.

30. X. Wang, W. Pu, R. Zhang, and F. Wei, "Inchworm-Like Soft Robot With Multi-Responsive Bilayer Films," *Biomimetics* 8 (2023): 443.

31. A. E. H. Chehade, B. Shen, C. M. Yakacki, T. D. Nguyen, and S. Govindjee, "Finite Element Modeling of Viscoelastic Liquid Crystal Elastomers," *International Journal for Numerical Methods in Engineering* 125 (2024): 7510.

32. M. Carlotti, O. Tricinci, F. Den Hoed, S. Palagi, and V. Mattoli, "Direct Laser Writing of Liquid Crystal Elastomers Oriented by a Horizontal Electric Field," *Open Research Europe* 1 (2021): 129.

Supporting Information

Additional supporting information can be found online in the Supporting Information section.

Supporting File 1: adfm75627-sup-0001-SuppMat.docx.

Supporting File 2: adfm75627-sup-0002-FigureS1-S3.zip.

Supporting File 3: adfm75627-sup-0003-VideoS1-S3.zip.